Desalination 623 (2026) 119849

Contents lists available at ScienceDirect

Desalination

journal homepage: www.elsevier.com/locate/desal

Beyond global metrics in capacitive water deionization: Position-resolved ion concentration from operando X-ray transmission

Max V. Rauscher [a], Richard Kohns [b,c], Malina Seyffertitz [a,1], Sebastian Stock [a], Sylvio Haas [c,d], Volker Presser [e,f,g], Christian Prehal [h], Nicola Hüsing [h], Oskar Paris [a,*]

[a] Department Physics, Mechanics and Electrical Engineering, Montanuniversität Leoben, 8700, Leoben, Austria
[b] Institute for Materials and X-Ray Physics, Hamburg University of Technology, 21073, Hamburg, Germany
[c] Centre for X-ray and Nano Science CXNS, Deutsches Elektronen-Synchrotron DESY, 22607, Hamburg, Germany
[d] Deutsches Elektronen-Synchrotron DESY, Notkestraße 85, 22607, Hamburg, Germany
[e] INM- Leibniz Institute for New Materials, Campus D2 2, 66123, Saarbrücken, Germany
[f] Department of Materials Science and Engineering, Saarland University, Campus D2 2, 66123, Saarbrücken, Germany
[g] Saarene - Saarland Center for Energy Materials and Sustainability, Campus C4 2, 66123, Saarbrücken, Germany
[h] Department of Chemistry and Physics of Materials, University of Salzburg, Jakob-Haringer Straße 2a, 5020, Salzburg, Austria

HIGHLIGHTS

- Operando X-ray transmission is a new methodology to map local concentrations in CDI devices.
- Flow-rate has a strong influence of on local concentration along the flow channel.
- Ionophobicity due to sub-nanometer pores is a dominant factor for overall CDI performance.

GRAPHICAL ABSTRACT

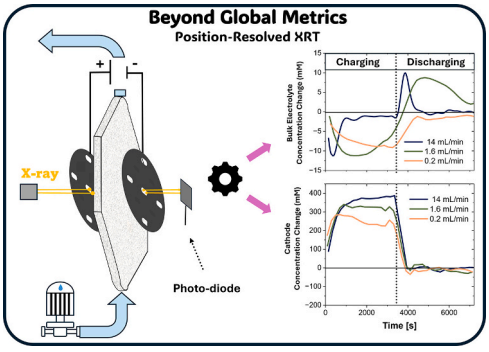

ARTICLE INFO

Keywords:
Desalination
CDI
Electrochemical water treatment
Operando X-ray imaging
Nanoporous carbon

ABSTRACT

The performance of novel electrode materials and the influence of cell geometry or flow rate on capacitive water deionization (CDI) are usually described by global metrics from the analysis of the effluent electrolyte together with the electrochemical response of the system. However, these approaches cannot provide information on local variations of ion concentration and related local efficiency within an operating device. Here, a novel approach of position-resolved operando synchrotron-based X-ray transmission is introduced to determine local ion concentration changes along the flow channel from the inlet (feedwater) to the outlet (effluent water) of a working CDI cell. A specific cell design allows the independent quantification of concentration changes within the bulk electrolyte in the flow channel as well as the two oppositely charged nanoporous electrodes. Results from a 15 mM CsCl feed solution using three flow rates and two carbon materials with hierarchical porosity reveal a

* Corresponding author.
E-mail address: oskar.paris@unileoben.ac.at (O. Paris).
[1] Now at: Yusuf Hamied Department of Chemistry, University of Cambridge, CB2 1EW Cambridge, United Kingdom.

https://doi.org/10.1016/j.desal.2026.119849
Received 22 October 2025; Received in revised form 28 November 2025; Accepted 3 January 2026
Available online 4 January 2026

complex spatial- and temporal ion distribution in the system. A distinct dependence of local concentration on the flow rate is observed, with generally decreasing local desalination capacity towards the outlet of the cell, particularly for slow flow rates. It is also found that a significantly better overall performance for one of the two materials can be related to dominant counter-ion adsorption within ultramicropores, which ions cannot access in their hydrated state at no applied potential (ionophobicity). Overall, the results demonstrate the unique potential of position-resolved operando X-ray techniques to get mechanistic insight into local ion redistribution in CDI systems, allowing ultimately guiding performance optimization.

1. Introduction

Freshwater scarcity is an escalating global challenge, especially in regions where conventional natural sources no longer meet the demand [1]. Current desalination technologies, such as reverse osmosis and multi-stage flash distillation, remain industrial standards. However, they are energy-intensive and best optimized for high-salinity seawater [2–5]. Among emerging alternatives, electrochemical desalination, in particular capacitive deionization (CDI), offers improved energy efficiency for low-salinity water, where it can even outperform reverse osmosis [1,2,6]. This makes CDI particularly attractive for brackish water desalination and sustainable water management in regions where low-salinity feedwater is available.

The fundamental ion removal mechanism in CDI is electric double layer (EDL) formation. EDL relies on the electrosorption of ions in nanopores of oppositely charged electrodes upon the application of an electric field, without involving charge transfer reactions. CDI predominantly utilizes carbon-based materials such as graphene, carbon nanotubes, carbon fibers, carbon foams, and biomass-derived (activated) carbons. These electrode systems are highly relevant due to their low cost and environmental compatibility, particularly when nanoporous carbons from biogenic sources with high electrical conductivity are employed [7–9].

CDI device performance is typically assessed by total salt removal normalized by electrode mass (less frequently by electrode volume or by electrode surface area) for comparison across systems [10]. Another often reported metric is the charge efficiency, which relates the amount of removed ions to the invested electric charge [11]. Established global metrics such as salt absorption capacity, charge efficiency, salt removal rate, water recovery, and stability are foundational for device comparison and design. However, they do not by themselves resolve local variations in ion concentration, charge efficiency, or transport pathways within porous electrodes. Recent work underscored the importance of ion transport kinetics, specifically how and where ions are stored, and the charge-balancing mechanisms at play [12–18]. These processes span multiple length-scales, from convective flow in the channel between the electrodes, to potential- and concentration gradient driven ion transport within macro- and mesopores, and sub-nanometer confinement effects that reorganize ions locally within micropores [19].

At the local scale of the micropores, three fundamentally different charge-balancing mechanisms govern global ion concentration changes: counter-ion adsorption (adsorption of oppositely charged ions, increasing the total ion concentration in the pores), co-ion expulsion (removal of like-charged ions, leading to a net concentration decrease), and ion exchange (simultaneous counter-ion entry and co-ion exit, leaving the ion concentration unchanged) [17,18]. The relative contribution of each mechanism is quantified by the charge efficiency, which in practice ranges from 1 (pure counter-ion adsorption) to 0 (pure ion exchange), and -1 (pure co-ion expulsion). For CDI, only counter-ion adsorption leads to a net removal of ions from the feedwater. Depending on the hydrated ion size, pores smaller than ~0.7 nm (ultramicropores [20]) can exhibit ionophobicity where hydrated ions are excluded from the pores due to steric hindrance [21–23]. Under an applied potential, partial dehydration enables counter-ion entry into these pores, enhancing charge efficiency (CE) and overall salt adsorption capacity (SAC). Therefore, this specific mechanism offers a potential route for selective counter-ion adsorption based on hydration energy and ion size [22,24]. In such ionophobic pores where exclusion dominates at open circuit, dehydration-driven entry also becomes a gatekeeper for ion selectivity. Tailoring micropore size (e.g by physical or chemical activation) can adjust such selectivity. It could be harnessed, for instance, for lithium extraction from brine water [25] or for the removal of radioactive- [26,27] and toxic elements [28].

Despite the conceptual simplicity of CDI, practical implementation reveals a complex interplay of transport, adsorption, and confinement effects across multiple length- and time scales [14,29,30]. Ion transport within real electrodes is influenced not only by pore size and topology, but also by surface interactions, tortuosity, and the dynamics of (de) hydration [19,31,32]. At the device level, flow dynamics and cell geometry introduce additional gradients that shape spatial ion distribution, often in ways that are not reflected in overall performance metrics [8,33,34].

While the theoretical understanding for such local mechanisms is well-developed for simple pore geometries such as slit pores, experimental validation, especially under operando flow conditions, remains limited [12,35]. Existing models assume idealized geometries, neglecting heterogeneity in pore connectivity and wettability found in real carbon structures. Modeling efforts, such as solving nonlinear dynamic models by Biesheuvel and Bazant [13] or further developed macroscopic continuum models [14,15,34], provide insight into spatial concentration gradients, but lack resolution at the pore scale.

In-situ small-angle X-ray scattering (SAXS) and X-ray transmission studies have offered valuable information on local concentration changes in supercapacitors [16–18,31]. However, similar approaches are still missing for CDI. Only a few neutron imaging results are available so far in this respect [33,36]. While neutron imaging may have advantages for the imaging of light ions (in particular Li^+ by employing different isotopes), it suffers from restricted time resolution and the strong incoherent scattering of water. Advantages of X-rays (in particular when using synchrotron radiation) are the much higher temporal and spatial resolution due to the high brilliance. Moreover, the possibility to easily change the X-ray energy permits in principle even to make use of the energy dependence of X-ray attenuation for ion-specific imaging. It is striking that despite the wide adoption of CDI, direct imaging of ion concentration dynamics within working electrochemical cells remains nearly unexplored.

In the present study, we introduce a straightforward approach based on position-resolved X-ray transmission measurements to directly obtain ion concentration gradients in a flow-by CDI cell under operando conditions. We employ CsCl as a model salt utilizing the high X-ray attenuation of Cs^+ as compared to Cl^-, making the results easier to interpret. Practical relevance is maintained through the use of a “quasi-standard” cell architecture, allowing real-time tracking of Cs^+ concentration changes, both in the flowing electrolyte and within the two porous electrodes separately. The objective of this study is to investigate how flow velocity, pore size, and architecture of the electrode materials influence spatially resolved ion concentration in the electrodes and in the flow channel. To this end, hierarchically structured carbons, featuring disordered macropores, ordered mesopores, and disordered micropores, are employed.

2. Materials and methods

2.1. Material preparation

Ordered mesoporous carbon materials (OMC) were synthesized via a soft-templating approach, followed by template removal through thermal oxidation at 280 °C for 1 h in 2 % O_2 / 98 % N_2, and carbonization at 850 °C for 2 h under nitrogen flow [37,38]. This procedure yields macroporous monoliths with a network of struts containing a hexagonally ordered structure of monodisperse cylindrical mesopores with a pore diameter of about 4 nm. Micropores are present within the walls of the mesopores and can be changed by targeted activation. Two different OMC samples were prepared to investigate the influence of volume and size distribution of micropores on CDI performance. The sample after pyrolysis at 850 °C without activation is referred to as OMC-0. OMC-2 was obtained by activating OMC-0 in a pure CO_2 atmosphere at 900 °C for 2 h to increase the specific surface area and pore volume of micropores without significant alterations of the mesopores.

The monolithic samples were manually ground in a mortar until a homogeneous fine powder was obtained. To fabricate electrodes, the powders were mixed with 10 mass% polytetrafluoroethylene (PTFE; 60 mass% solution in water, Sigma-Aldrich) as a binder. Ethanol was added before PTFE incorporation to improve dispersion. The mixture was then stirred until a malleable, viscoelastic consistency was achieved. The mixture was rolled to a thickness of 200 µm, and 32 mm diameter circular electrodes were punched out. The aqueous electrolyte was prepared by dissolving CsCl (99.9 %, Sigma-Aldrich) in Milli-Q water. The electrode mass for OMC-2 was 70.7 mg and for OMC-0 96.5 mg.

2.2. Material characterization

Pore structure and specific surface area were derived from N_2 (77 K) and CO_2 (273.15 K) gas sorption analysis (GSA) using an Autosorb IQ system (Anton Paar QuantaTec, Inc.). Electrode samples were degassed at 120 °C for 24 h prior to analysis. BET surface area was calculated in the relative pressure range 0.05–0.3 following ISO 9277:2022. Pore size distributions were calculated from the adsorption branch using a QSDFT-based kernel with slit/cylindrical pore assumptions for the N_2 data [39]. For the CO_2 data, a grand canonical Monte Carlo-based kernel was used [40].

The specific cumulative pore volumes from the N_2 and CO_2 adsorption data as a function of the pore size are depicted in Fig. 1a and Fig. 1b, respectively. Micropore and mesopore volumes were distinguished according to IUPAC recommendations [20], using a 2 nm threshold as depicted in Fig. 1a. A distinct plateau in the cumulative pore volume (Fig. 1a) indicates the clear separation between micro- and mesopores, with the micropores being smaller than 1 nm and the mesopores being larger than 3 nm. The specific micropore volume was taken from the value of the first plateau, while the specific micro + mesopore volume refers to pore volume (V_p) estimated from the N_2 adsorption isotherms using the Gurvich rule at $p/p_0 = 0.95$. The activation step increases the micropore volume by a factor of 2.4 (Fig. 1a), and the specific (*BET*) surface area increases by roughly a factor of 2 (Table 1). However, the CO_2 adsorption data in Fig. 1b demonstrate that the non-activated sample has a considerably higher fraction of ultramicropores (< 0.7 nm) in the micropore volume, as compared to the activated sample. The volume fraction of ultramicropores in the micropores ($\varphi_{Ultramicro}$) is reported in Table 1. This means that activation not only creates new micropores, but it also likely leads to the growth/coalescence of the already existing ones.

The total specific pore volume of the electrodes was calculated from their known volume and mass after correction for the contribution of the binder. The macropore volume was estimated by subtracting the micro- and mesopore volume from N_2 gas sorption and the skeletal carbon volume from the total electrode volume. Pore volume fractions (porosities) were calculated using a skeletal carbon density of 2 g/cm^3 and are listed in Table 1. These data provide a quantitative basis for evaluating the X-ray transmission data.

The mean mesopore diameter D_{Meso} was obtained from the differential pore size distribution from N_2 gas sorption, assuming cylindrical mesopores (*Supporting Information*, Fig. S1) and the respective values are listed in Table 1. Corresponding size distributions from CO_2 adsorption are shown in *Supporting Information*, Fig. S2.

The electrodes were also characterized using SAXS at the (SAXMAT) beamline P62 at DESY [41] at an X-ray energy of 11 keV with an Eiger2 X9M detector (*Supporting Information*, Fig. S3). The mesopore distance was calculated from the (10) Bragg peak resulting from the 2D hexagonal pore ordering [37,42]. The corresponding lattice parameters *a* (i.e., the distance between adjacent cylindrical mesopores) for OMC-0 and OMC-2 are also listed in Table 1, indicating a slight overall shrinking due to the activation treatment, while the mesopore diameter increases slightly. The differences between the two samples concerning meso- and macropores (Table 1) are small and can be considered negligible with regard to ion transport properties. Therefore, the relevant differences between the two samples for the present work are the considerably larger micropore volume and specific surface of OMC-2 (Table 1), and a

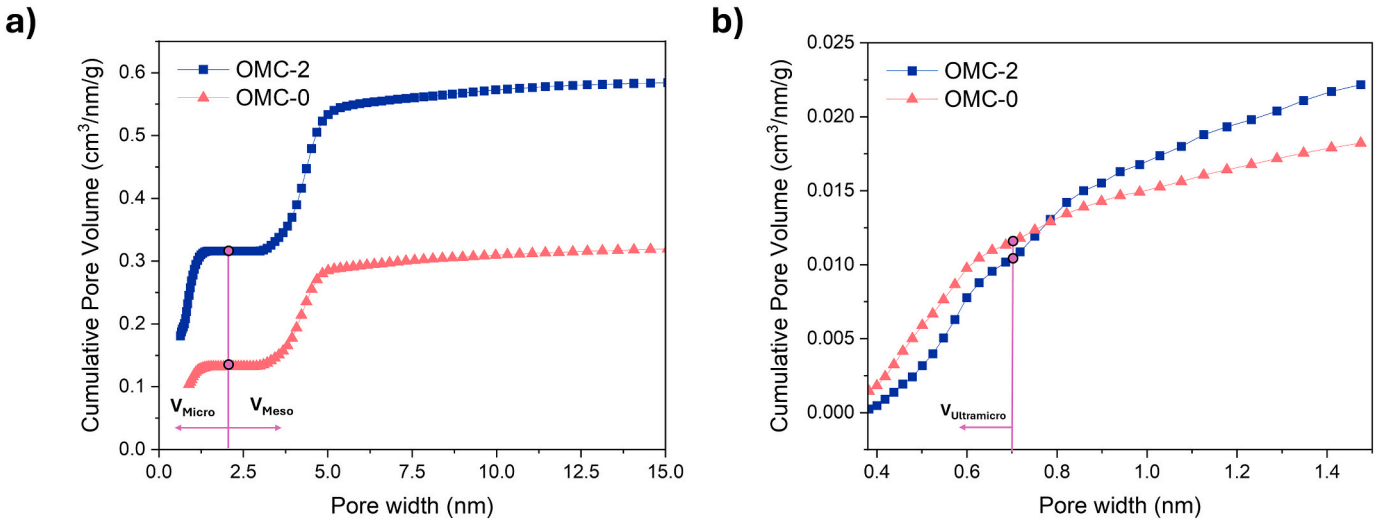

Fig. 1. Cumulative pore volume as a function of pore size from a) N_2 gas sorption at 77 K (quenched solid density functional theory, slit/cylinder pores adsorption branch) and b) CO_2 gas sorption 273 K (Monte-Carlo model for slit pores).

Table 1
Pore volume fractions (porosities) φ, specific surface area S_{BET}, specific pore volume V_p, and mean mesopore diameter D_{Meso} calculated from nitrogen gas sorption for both electrodes. The fraction of ultramicropores (<0.7 nm) relates to the fraction of micropores (<2 nm) rather than the total fraction of pores. The pore mesopore distance a was obtained from the 10 Bragg reflection from the mesopore lattice measured with SAXS.

	φ_{Micro} (%)	φ_{Meso} (%)	φ_{Macro} (%)	S_{BET} (m^2/g)	V_p (cm^3/g)	$\varphi_{Ultramicro}$ (%)	D_{Meso} (nm)	a (nm)
OMC-0	8.5	11.2	46.0	514	0.338	73.0	4.36	10.4
OMC-2	14.9	12.2	47.8	1074	0.609	45.9	4.50	10.1

larger amount of very small micropores in OMC-0 (Fig. 1b and *Supporting Information*, Fig. S3). The increased amount of micropores in OMC-2 may also influence the connectivity of the ordered cylindrical mesopores due to micropore channels between the mesopores. Additional structural analysis can be found in the Supplementary Information in Fig. S5b): X-ray diffraction (XRD), Fig. S6): scanning electron microscopy (SEM) and Fig. S7): transmission electron microscopy (TEM).

2.3. Electrochemical flow cell

A custom-built electrochemical CDI cell was used for position-resolved in-situ X-ray transmission experiments (Fig. 2). The principal cell design is based on previously established in-situ SAXS/WAXS electrochemical setups for supercapacitors [17,18,31]. It features an all-metal housing made of titanium to ensure electrochemical stability. The working electrodes were positioned directly on thin Pt current collectors attached to polyimide (Kapton) X-ray windows. A custom 3D-printed polyethylene terephthalate glycol (PET-G) flow guide was inserted between the electrodes to regulate electrolyte flow. Five layers of Whatman GF/A separators were stacked within the flow channel, shaped to match the flow guide geometry (*Supporting Information*, Fig. S4). A separator-free entrance region was included to homogenize pressure following guidance from pressure drop simulations [43]. It also features an entrance and exit reservoir (Fig. 2c). The total cell volume is roughly 3 mL, while the active volume between the electrodes is about 1.5 mL.

2.4. Position-resolved X-ray transmission measurements

To study local ion concentration at multiple positions, scanning X-ray transmission (XRT) measurements along with SAXS/WAXS were performed at the beamline P62 (SAXSMAT) at the synchrotron radiation facility PETRA III at DESY in Hamburg. Only the transmission measurements are considered here. Specially designed electrodes with precisely aligned and laterally shifted perforations were used, as shown in Fig. 2a. This design enabled the acquisition of independent data from both electrodes and the bulk electrolyte in the flow channel within a small area. To this end, two adjacent 2 mm holes were punched into each electrode. Removing the material in between resulted in an elongated opening of 6 mm × 2 mm (Fig. 2b), with regions containing only the separator without electrodes (white part in the middle) and either of the

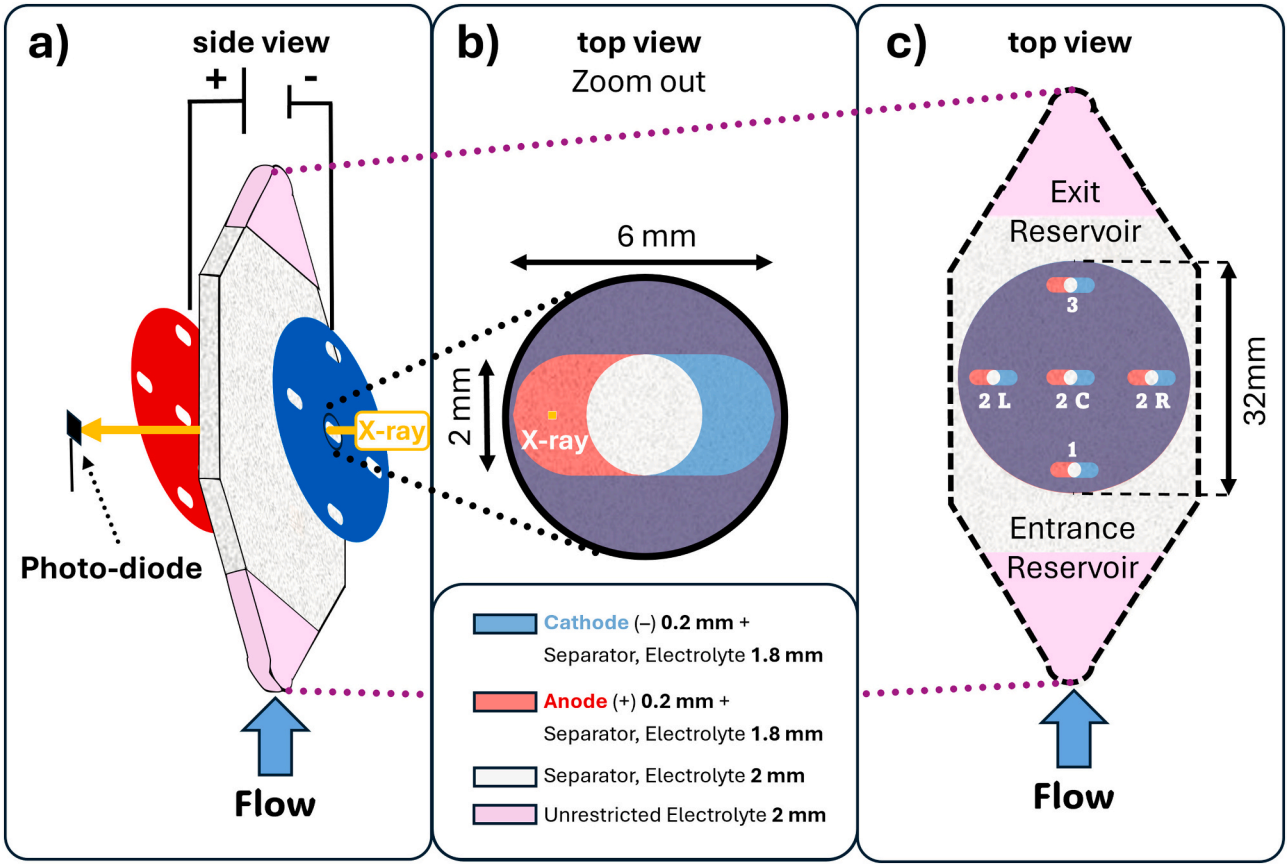

Fig. 2. Sketches of the electrode/separator assembly with aligned and laterally shifted "hole configurations". a) side view, b) zoomed top view and c) top view. Highlighted in b) in yellow is the X-ray beam with quadratic cross-section of 240 µm edge length and the yellow arrow in a) shows the direction of the X-ray irradiation. (For interpretation of the references to colour in this figure legend, the reader is referred to the web version of this article.)

two electrodes (red and blue parts) plus the separator. In total, five such points of interest (POI) were designed (Fig. 2c) that could each be scanned with a small X-ray beam (yellow spot in Fig. 2b). The five POIs numbered in Fig. 2c) were actively measured by scanning the X-ray beam horizontally at each POI (inlet: POI 1, middle left: POI 2-L, middle center: POI 2-C, middle right: POI 2-R, and outlet: POI 3).

XRT measurements were carried out using a 15 mM CsCl aqueous feed solution at flow rates of 0.2 mL/min, 1.6 mL/min, and 14 mL/min. The slowest flow rate can be considered close to conditions in supercapacitors ("quasi-static" reservoir within the timeframe of charging used here), while the highest flow rate would be more closely resembling an unlimited reservoir (constant concentration) due to high replenishing rates. Given the total active volume of the cell being ≈1.5 mL, the chosen flow rates are reasonable values for very slow ("quasi-static"), intermediate (standard operating regime), and fast flow. Desalination cycling was performed by chronoamperometry, that is, charging by applying a voltage step from 0 V to 1 V and holding for 3600 s, followed by discharging at 0 V for another 3600 s. For each flow rate, two consecutive charge/discharge cycles were measured. To minimize transient effects, each cell underwent 6–8 ex-situ pre-conditioning cycles before the actual measurement [10]. The X-ray energy was 11 keV, and the size of the X-ray beam (quadratic cross section) was 0.24 mm.

The samples were scanned across the X-ray beam with transmission measurements at 13 positions for each POI to reduce radiation damage and to capture local heterogeneity. To avoid cross-talk from the electrolyte opening, we excluded points immediately adjacent to the separator-only region. To avoid hitting both electrodes, the outermost points were also excluded. For each region (anode, electrolyte, cathode), we therefore report a single scanning point per POI: the point farthest from the opening that is not at the outer edge. This conservative selection improves the spatial specificity of electrode- and electrolyte-resolved signals.

Voltage cycling and electric current measurement were performed using a Gamry REF 600 or an Interface 1010B potentiostat. They were used alternately during a measurement, while the second cell was conditioned. Effluent conductivity was recorded using a VWR CO3100L conductivity meter and converted to concentration via a calibration procedure similar to Ref. [10].

2.5. Calculation of the ion concentration changes from XRT

The transmission of X-rays through a material follows Lambert-Beer's law, $\tau = exp(-\mu d)$, where μ is the material-specific and X-ray energy-dependent linear attenuation coefficient, and d is the sample thickness. To calculate ion concentration changes in the bulk electrolyte (white region in Fig. 2b), the linear attenuation coefficient μ is expressed as a sum of contributions from individual anions, cations, and water, weighted by their respective attenuation contribution. This yields for a CsCl aqueous solution Eq. (1) [16]:

$$\begin{aligned} ln(\tau_{el}) &= ln(\tau_{el+\mathrm{cell}}) - ln(\tau_{\mathrm{cell}}) \\ &= -d_{el}\left[c_{Cs}M_{Cs}\left(\frac{\mu}{\rho}\right)_{Cs} + c_{Cl}M_{Cl}\left(\frac{\mu}{\rho}\right)_{Cl} + c_{H_2O}M_{H_2O}\left(\frac{\mu}{\rho}\right)_{H_2O}\right] \end{aligned} \quad (1)$$

where d_{el} represents the total electrolyte thickness and $M_i\ (\mu/\rho)_i$ are the molar attenuation cross sections. The solvent contribution is described by the bulk density of water $\rho_{H_2O} = c_{H_2O}M_{H_2O}$ multiplied by its mass attenuation coefficient $(\mu/\rho)H_2O$. A different density of water in the hydration shells of the ions must, in principle, also be considered. However, since ion concentrations are low and the attenuation of water is generally much weaker than that of the used ions (Table 2), this influence is neglected here. The cell components (i.e., the separator, Pt current collectors, and polyimide windows) contribute a constant attenuation, denoted as τ_{cell}, which is independently measured and assumed to remain unchanged throughout the experiment.

Table 2 shows that even though the molar attenuation cross-section of water is small, most of the attenuation in the cell still comes from water due to the very low ion concentration. Therefore, only small changes in the transmission τ_{el} are expected, requiring high measurement accuracy. When both electrode perforations are completely filled with electrolyte, d_{el} in Eq. (1) represents the geometrical distance between the two current collectors. This value is corrected for the volume fraction occupied by the separator (Fig. 2b). However, some small variations in electrolyte thickness across the device cannot be excluded due to electrode inhomogeneities and bulging of the Kapton windows during flow. Therefore, the effective X-ray path length between the entrance and the exit polyimide windows, d, was estimated from the WAXS data using the split Bragg reflections from the two Pt current collectors, which were directly attached to the Kapton windows (*Supporting Information*, Fig. S5 and Eq. (S1)). The procedure and the numerical values used in all further calculations of the electrolyte thickness are given in *Supporting Information*, Table S1. The WAXS-derived values agree well with the nominal value of 2 mm, but the observed trend towards smaller d with decreasing flow rate suggests a flow-rate-dependent bulging of the cell.

Table 2
Molar attenuation coefficients μ/ρ^*M as well as cell-inlet molar concentrations c and resulting linear attenuation coefficients. Values for (μ/ρ) were taken from Ref. [48] and were extrapolated for 11 keV.

	μ/ρ^*M (cm^2/mol)	c (mol/cm^3)	μ (cm^{-1})
H_2O	69.41	$55.5{\cdot}10^{-3}$	3.852
Cl	1506.20	$15{\cdot}10^{-6}$	0.023
Cs	18,059.19	$15{\cdot}10^{-6}$	0.271

The separator thickness d_{Sep} was determined by measuring the transmission of the cell without electrolyte (with and without separator). For the linear attenuation coefficient of the separator, pure SiO_2 with a density of 2.3 g/cm^3 was assumed. Calculation of d_{Sep} from the transmission yielded a thickness of 200 µm, which was subtracted from the geometric thickness d (Table S1) to give the effective electrolyte thickness $d_{el} = d - d_{Sep}$.

When the X-ray beam passes through one of the electrodes (red or blue regions in Fig. 2b), the interpretation of the XRT signal becomes more complex. The majority of the X-ray absorption still originates from the bulk electrolyte, given the nominally 1.8 mm flow channel versus 0.2 mm electrode thickness (Fig. 2). We attribute additionally the macroporosity of the electrodes (almost 50 %, Table 1) to the bulk electrolyte, since no relevant ion adsorption in the macropores is expected to take place. The concentration of ions in the meso- and micropores of one of the electrodes (denoted with the subscript "E", to be distinguished from the bulk electrolyte with subscript "el") is then determined by subtracting the bulk electrolyte contribution from Eq. (1) for a corrected thickness of $d_{el}^{'} = d_{el} - d_E^{'}$, *with* $d_E^{'} = d_E(\varphi_{Meso} + \varphi_{Micro})$ being the geometric electrode thickness d_E corrected for the macropore volume and the volume of the solid carbon skeleton. This yields the following equation for the transmission of an electrode τ_E:

$$\begin{aligned} ln(\tau_E) &= ln(\tau_{E+el+\mathrm{cell}}) - \frac{d_{el}^{'}}{d_{el}} ln(\tau_{el}) - ln(\tau_{\mathrm{cell}}) \\ &= -d_E^{'}\left[c_{Cs}^{E}M_{Cs}\left(\frac{\mu}{\rho}\right)_{Cs} + c_{Cl}^{E}M_{Cl}\left(\frac{\mu}{\rho}\right)_{Cl} + c_{H_2O}M_{H_2O}\left(\frac{\mu}{\rho}\right)_{H_2O}\right] \\ &\quad - d_C\rho_C\left(\frac{\mu}{\rho}\right)_C \end{aligned} \quad (2)$$

with the last term on the right side being the attenuation of the carbon with effective thickness d_C.

The total ion concentration in the electrodes at no applied potential is a priori unknown and can differ from the bulk electrolyte solution in the flow channel [44,45]. We assume that at 0 V, the concentration of anions and cations is the same also in the pores. Moreover, because τ_{cell} and the carbon electrode contributions ($d_C\,\rho_C\left(\frac{\mu}{\rho}\right)_C$) were not measured

independently, absolute ion concentrations according to Eqs. (1)–(2) could not be reliably determined. Therefore, only changes in the X-ray transmission were analyzed relative to a reference state (τ_{ref}), chosen as the transmission immediately before the first charging step for both consecutive cycles at that flow rate. This procedure also effectively eliminates all constant contributions from the solid cell material, which can be assumed to be constant. Under the additional assumption that water density remains constant in the bulk electrolyte (el) and in the micro- and mesopores in the electrodes (E), Eqs. (3)–(4) follow:

$$ln(\Delta\tau_{el}) = ln(\tau_{el}) - ln(\tau_{ref,el}) = -d_{el}\left[\Delta c_{Cs} M_{Cs}\left(\frac{\mu}{\rho}\right)_{Cs} + \Delta c_{Cl} M_{Cl}\left(\frac{\mu}{\rho}\right)_{Cl}\right] \quad (3)$$

$$ln(\Delta\tau_E) = ln(\tau_{E+el}) - ln(\tau_{ref,E+el}) - \frac{d_{el}^{'}}{d_{el}} ln(\Delta\tau_{el}) = -d_E^{'}\left[\Delta c_{Cs}^{E} M_{Cs}\left(\frac{\mu}{\rho}\right)_{Cs} + \Delta c_{Cl}^{E} M_{Cl}\left(\frac{\mu}{\rho}\right)_{Cl}\right] \quad (4)$$

Charge neutrality in the bulk electrolyte leads to further simplification of Eq. (3), yielding $\Delta c_{Cs} = \Delta c_{Cl} = \Delta c$ and allowing to unambiguously determine the bulk electrolyte concentration change (*Supporting Information*, Eq. (S2)). This is generally not possible for the electrodes, since Cs^+ and Cl^- contribute in an unknown way to the XRT signal. If we assume that the concentration change of Cl^- is not dominating (i.e., $\Delta c_{Cl}^{E} \leq \Delta c_{Cs}^{E}$), its contribution to Eq. (4) may be neglected due to the much higher molar attenuation cross-section of Cs^+ (Table 2). The corresponding simplified equation is given in *Supporting Information*, Eq. (S3).

For the low concentrations investigated here, counter-ion adsorption and/or ion exchange can be assumed to be dominant charge-balancing mechanisms. Therefore, the approximation Eq. (S3) should hold well for the negatively charged electrode (cathode), giving a direct good estimate for the Cs^+ concentration change. However, for the positively charged electrode (anode), the situation is more complex, since only pure counter-ion adsorption would deliver the Cl^- concentration change (*Supporting Information*, Eq. (S4)). At the same time, already minor mobilization of Cs^+ would give a non-negligible Cs^+ contribution. Therefore, interpreting changes in the anode concentration is more difficult.

3. Results and discussion

3.1. Ion concentration changes during cycling

Fig. 3 shows an example of concentration changes under the assumption that only Cs^+ contributes to the transmission in the electrodes (*Supporting Information*, Eq. (S2–S3)) for the bulk electrolyte (a), the cathode (b), and the anode (c). Respective curves for all other points of interest (POIs, Fig. 2) are shown in *Supporting Information*, Figs. S8–S17. All data were measured for two subsequent charge/discharge cycles. The majority of measurements show high reproducibility with only small variation between the two cycles. However, some datasets (*Supporting Information*, Table S2) had to be excluded from the

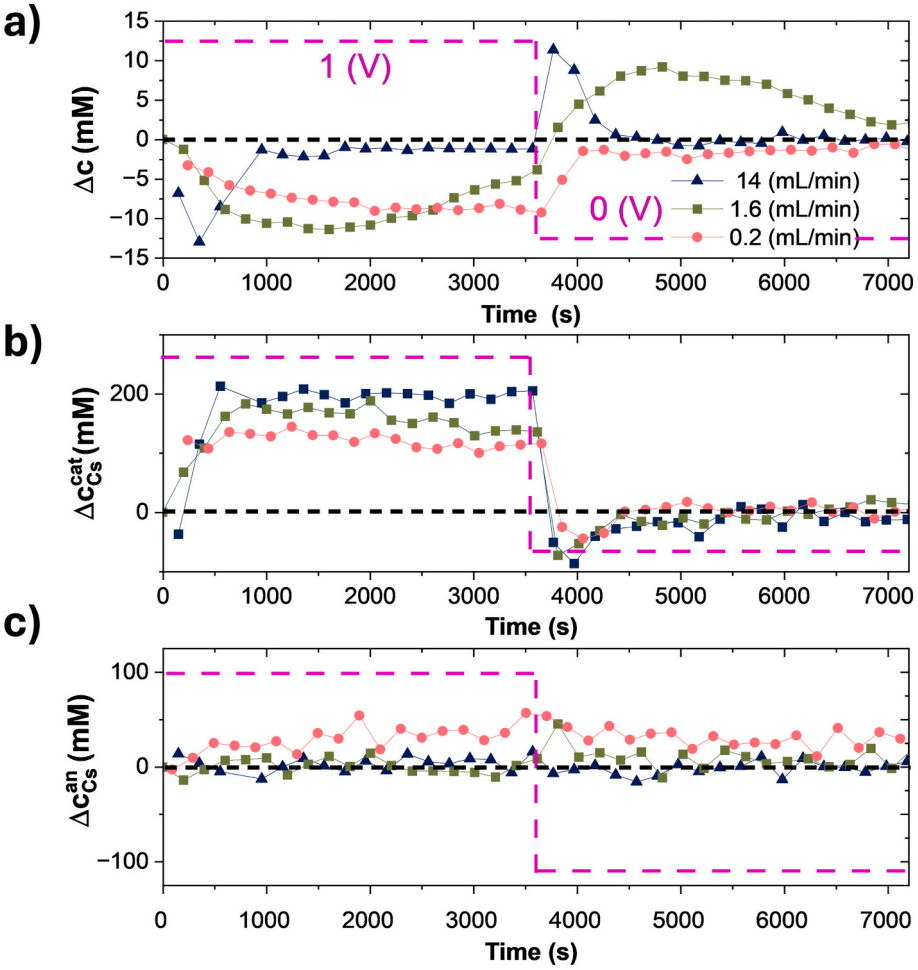

Fig. 3. Cs^+ concentration changes for sample OMC-2 for all flow rates and the first cycle at the central hole of the cell, POI 2 (center). a) bulk electrolyte concentration in the flow channel, b) Cs^+ concentration in the cathode, c) Cs^+ concentration in the anode. The applied voltage is indicated by the dashed pink line (1 V: 0–3600 s, 0 V: 3600–7200 s). (For interpretation of the references to colour in this figure legend, the reader is referred to the web version of this article.)

analysis due to significant deviations (presumably due to moving air bubbles or other local heterogeneities in the system).

Fig. 3a shows the concentration change in the bulk electrolyte at POI 2-C, that is, the central hole in the middle of the cell (Fig. 2). A strong negative initial concentration change is observed for all three flow rates. For the fastest flow rate, Δc has returned to zero after about 1000 s, indicating that after this time the bulk electrolyte concentration matches the feedwater concentration with no further desalination taking place. For the intermediate flow rate of 1.6 mL/min, a maximum negative Δc is reached after about 1500 s, and eventually Δc approaches approximately zero after 1 h. At the slowest flow rate of 0.2 mL/min, Δc becomes increasingly negative over the first 2000 s and remains then roughly constant, with no tendency to decrease throughout the whole charging regime. After the voltage is set back to zero, the bulk water concentration changes for all three flow rates. For the higher flow rate, the concentration change is initially positive, and returns then to zero, similar to the charging regime as expected for a full discharging of the previously charged electrodes. For the intermediate flow rate, the discharging process takes much longer and is almost complete after 1 h. In contrast, for the slowest flow rate, the initially negative Δc returns to zero quickly without becoming positive at any point in time, confirming a "quasi-static" condition. Similar, yet quantitatively different changes are observed for the other POIs (*Supporting Information*, Figs. S8–S17), indicating complex time-dependent concentration gradients in the flow channel.

The Cs^+ concentration change in the negatively charged electrode (cathode) is shown in Fig. 3b. For all three flow rates, the stored Cs^+ concentration reaches a roughly constant value after 1000 s. But the absolute values are different: 200 mM for the fastest, and almost a factor of 2 smaller for the slowest flow rate, the intermediate flow rate lying in between. This is consistent with the behavior in the bulk electrolyte which is not reaching zero at the end of the charging cycle (Fig. 3a), suggesting that, at the two slow flow rates, ion rearrangement continues after 1 h. The almost constant (and in some cases even slightly decreasing) Cs^+ concentration at the cathode points towards slow processes of (partly competing) ion adsorption and redistribution within the electrode. This is probably because the flow velocity of the electrolyte in the channel and ion transport velocities due to electrical potential gradients and concentration gradients between the electrodes and into the nanopores are of the same order of magnitude. This leads to a complex spatial and temporal distribution of ions in the system, as seen by the varying behavior at different POIs (*Supporting Information*, Figs. S8–S17). Interestingly, upon returning to zero applied voltage, the Cs^+ concentration exhibits a transient dip before equilibrating to values identical to those observed prior to cycling. This might be interpreted as co-ion expulsion with subsequent equilibration, similarly as already reported by Prehal et al. 2018 [16].

The changes in the positively charged electrode (anode) are more difficult to interpret. In the case of pure counter-ion adsorption, the Cs^+ concentration change in the anode would be zero, and the changes would be given by the Cl^- concentration change (*Supporting Information*, Eq. (S4)). Conversely, if Cs^+ contributes to the charge balancing similarly to Cl^- (i.e., ion exchange), the transmission would be dominated by Cs^+ (*Supporting Information*, Eq. (S3)). Fig. 3c shows hardly any change for the two faster flow rates and a positive concentration change for the slowest flow rate, and is not very conclusive in this respect. However, several other POIs (*Supporting Information*, Figs. S8c–S17c) show an initially clearly negative concentration change. Although the assumption of dominating Cs^+ contribution to the signal does not necessarily hold for the anode, it is clear that any increase in Cl^- concentration within the anode as compared to the 0 V state would lead to a positive concentration change. Since approximately 12 Cl^- ions would result in the same XRT change as one Cs^+ ion (Table 2), an initial negative concentration change for the first 1000 s indicates that Cs^+ must be strongly involved at this stage of charging. This suggests initially ion exchange or even co-ion expulsion as a dominating mechanism. In addition, the magnitude of the concentration changes at the anode (up to −100 mM, *Supporting Information*, Fig. S12c and Fig. S14c) implies that the ion concentration in the meso- and micropores at 0 V must be significantly higher than the feedwater concentration (15 mM). After the initial period, the signal returns to the baseline, or becomes even slightly positive, probably driven by subsequent Cl^- adsorption (*Supporting Information*, Figs. S8c–S17c). Further elaboration of why the anode side cannot be evaluated is detailed in the Supplementary Information.

We will, at this point, not further consider the complex time and position-dependent concentration changes, as many different aspects influence them. In the following, we analyze the final concentration changes at the end of each charging cycle in more detail. For all measured data points, an almost constant Cs^+ concentration is reached in the cathode after 1 h holding time (Fig. 3b and *Supporting Information*, Figs. S8b–S17b).

3.2. Spatial dependence and flow rate dependence of ion concentrations

Fig. 4 depicts the bulk electrolyte concentration changes averaged over the last 10 min of the two 1 h charging cycles as a function of position. At the fastest flow rate of 14 mL/min, the electrolyte concentration returns essentially to its initial value for all POIs after 1 h. This is no longer the case at lower flow rates. At 1.6 mL/min, a strong gradient is observed across POI 1 (inlet), POI 2 (average of the 3 middle POIs 2-L, 2-C and 2-R), and POI 3 (outlet). Similar is true for 0.2 mL/min, where not even at the inlet POI $\Delta\bar{c}$ does return to zero. Interestingly, for the OMC-0 sample, the concentration change is $\Delta\bar{c} \approx -12$ mM for the outlet hole (POI 3) for both slow flowrates, while it is considerably smaller for sample OMC-2. This suggests a strong influence of the nanopore structure on the ion dynamics under otherwise identical conditions. Except for this specific difference, the two electrode materials lead to similar final concentration profiles for the two materials for the different flow rates.

Fig. 5 shows the corresponding Cs^+ concentration changes at the end of the charging process in the negatively charged electrode. Consistent with the bulk electrolyte concentration decrease, the Cs^+ concentration

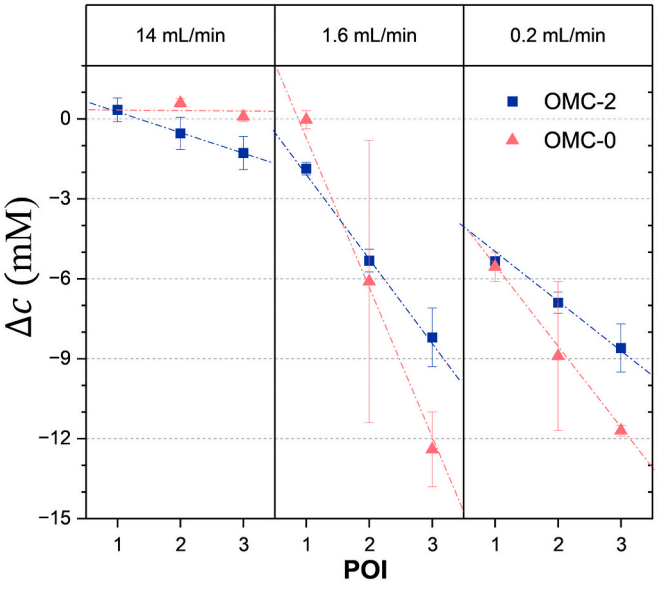

Fig. 4. Position-dependent final concentration changes in the bulk electrolyte for both materials and all three flow rates. Positions are according to Fig. 2: POI 1 close to the inlet, POI 2 in the middle of the cell, and POI 3 close to the outlet. The three holes in the (2-L: left, 2-C: center, 2-R: right) are averaged. Guides for the eye are depicted as dashed-dotted lines (blue OMC-2, red OMC-0). (For interpretation of the references to colour in this figure legend, the reader is referred to the web version of this article.)

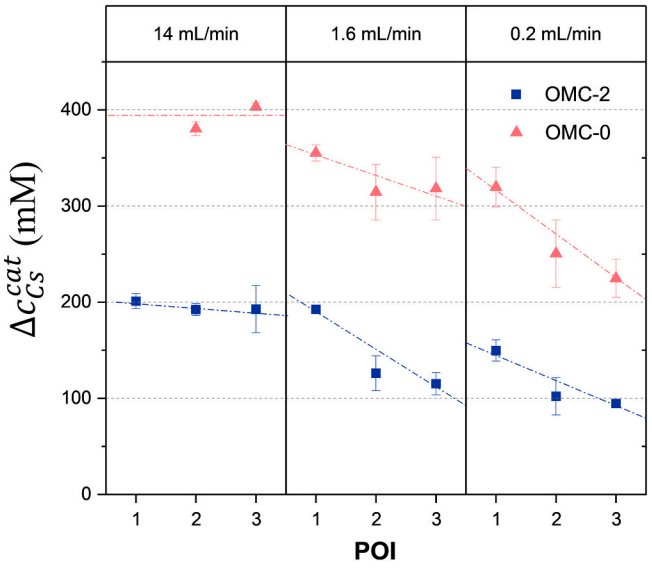

Fig. 5. Average Cs^+ concentration changes for the cathode Δc_{Cs}^{cat}, for both materials and all three flow rates. Positions are according to Fig. 2: POI 1 close to the inlet, POI 2 (average of 2-L: left, 2-C: center, 2-R: right) in the middle of the cell, and POI 3 close to the outlet. Guides for the eye are depicted as dashed-dotted lines (blue OMC-2, red OMC-0). (For interpretation of the references to colour in this figure legend, the reader is referred to the web version of this article.)

in the cathode is increased. Most remarkably, the overall concentration increase in the electrodes is considerably higher for the OMC-0 sample for all flow rates at all POIs by roughly a factor of 2. While for the fastest flow rate, the electrode concentrations are similar along the flow channel at the different POIs, for the two slower flow rates, the inlet (POI 1) exhibits consistently higher ion concentration as compared to the middle (POI 2) and the outlet (POI 3) positions for both samples. We attribute this to higher ion supply close to the inlet, with the significant reduction of stored ions in the center and towards the outlet, pointing towards increased ion exchange instead of counter-ion adsorption due to reduced flow rate as well as longer contact time between the electrolyte and electrode and reduced ion supply.

We note the high standard deviation for OMC-0 at the middle cell position (POI 2), particularly in Fig. 4. In order to compare overall trends, the data for the POIs 2-L, 2-C and 2-R were averaged and the standard deviation was given as error bar, even though $\Delta\bar{c}$ values were quite different despite their similar distance from the inlet (see Fig. S18 and the individual data in Figs. S14–16). The origin of this lateral deviation is unknown. For all three flow rates, the same cell was used for the XRT experiments in the sequence, as shown in Fig. 4–5 (i.e., from high to low flow rate). We attribute the large deviation in the OMC-0 electrode tentatively to a local artefact of this specific cell, since otherwise at least some related tendency should also be seen in the OMC-2 cell. This underlines the importance of a highly reproducible cell design and optimization when studying local effects in the future.

3.3. Global metrics

To validate our approach of determining local ion concentration changes using XRT, we calculate the so-called charge efficiency (CE) η and the salt adsorption capacity (SAC). The SAC is defined as the amount of adsorbed salt during a charging cycle divided by the electrode mass, usually given in mg/g: $SAC = \frac{N_{ad}}{m_{el}} * M_{CsCl}$, where N_{ad} is the number of adsorbed moles, m_{el} is the electrode mass and M_{CsCl} is the molar mass of CsCl. The charge efficiency is the ratio between N_{ad}, and the total (electronic) charge Q invested: $\eta = \frac{N_{ad}}{Q^* F}$, where F is the Faraday constant. Q was obtained by integrating the recorded electric current over time after correcting for leakage current, as detailed in Ref. [10]. From the conductivity measurement of the effluent solution $N_{ad,cond}$ was determined using a calibration procedure according to Ref. [10], and the corresponding CE η_{cond} and SAC_{cond} were calculated. In order to determine the adsorbed moles of ions from the X-ray transmission measurements ($N_{ad,X\text{-}ray}$) the Cs^+ concentration change (Δc^-_{Cs}) was multiplied by the total (micropore + mesopore) volume, times two assuming equilibrium charge on both electrodes. To compare the global metrics SAC_{cond} and η_{cond} with the local transmission measurements, the average value and standard deviation of $N_{ad,X\text{-}ray}$ from the last 10 min of charging was averaged over all 5 POIs in order to calculate the x-ray derived global metrics $\eta_{X\text{-}ray}$ and $SAC_{X\text{-}ray}$. The results of the global metrics are summarized in Table 3, showing agreement for the fast flow rate between the two methods, thus confirming the robustness of the X-ray-based approach. For the intermediate flow rate, the differences are larger, and only the trend is consistent between the two methods. For the slowest flow rate, the CE based on electrical conductivity could not be determined due to the limited sensitivity of the instrument. The main results from the analysis of the position resolved ion concentrations in the electrodes (Fig. 5) and the CE as an important performance metric for CDI (Table 3) are summarized as follows:

i) the CE and SAC decreases as flow rate decreases, indicating transport limitations at lower electrolyte flow;
ii) OMC-0 consistently outperforms OMC-2 demonstrating a considerably higher SAC and also a higher CE of this material. It shows that the higher Cs^+ uptake of OMC-0 persists despite its lower total micropore volume, scaling consistently with the ultramicropore fraction in the micropores rather than total micropore volume (Table 1). Findings from Nuclear Magnetic Resonance Spectroscopy and Molecular Dynamics Simulations detailed in Bi et al. [22] correlate well with the observations reported here. It highlights the importance of ultramicropore fraction in activated carbons for high charge efficiency even at very low flow rates. In the following section we discuss the influence of local replenishment and time on the global metrics and separate the ionophobic contribution from other mechanisms.

3.4. Replenishment-limited efficiency and timescale-separated ion transport

With our operando scanning X-ray transmission data, we have quantified local Cs^+ ion concentration changes in the bulk electrolyte within the flow channel as well as in the negative electrode of a working CDI device. Since Cs^+ exhibits a much higher X-ray attenuation coefficient as compared to Cl^- and water, the XRT signal is dominated by Cs^+ as long as Cl^- concentration changes are not dominant. This is assumed to be the case for the negatively charged electrode and is used to

Table 3
Charge efficiency (CE) and salt adsorption capacity (SAC) values from X-ray transmission and conductivity measurement of effluent solution.

	OMC-0	OMC-2	OMC-0	OMC-2
	η_{X-ray}	η_{X-ray}	η_{cond}	η_{cond}
14 (mL/min)	1.01 ± 0.03	0.70 ± 0.04	0.99 ± 0.025	0.66 ± 0.025
1.6 (mL/min)	0.86 ± 0.07	0.50 ± 0.1	0.38 ± 0.025	0.14 ± 0.025
0.2 (mL/min)	0.69 ± 0.1	0.40 ± 0.08	-	-

	SAC_{x-ray} (mg/g)	SAC_{x-ray} (mg/g)	SAC_{cond} (mg/g)	SAC_{cond} (mg/g)
14 (mL/min)	44.9 ± 1.3	37.6 ± 1.5	41.4 ± 1.0	38.6 ± 1.0
1.6 (mL/min)	37.8 ± 2.6	27.9 ± 2.8	15.8 ± 1.0	7.4 ± 1.0
0.2 (mL/min)	30.4 ± 3.0	30.4 ± 2.4	-	-

quantitatively estimate cation concentration changes in the system. While for the fastest flow rate, ion concentration profiles were found to become quite homogeneous within a short time, slower flow rates result in a complex, time-dependent, and position-dependent distribution of ions in the electrodes and in the flow channel.

This emphasizes the importance of considering several different time scales at play, related to i) the macroscopic forced electrolyte flow in the flow channel, ii) the ion migration between the electrodes and into the nanopores driven by the gradient of the electric potential, and iii) diffusive transport of ions along concentration gradients. A particularly interesting result in this respect is the significantly higher Cs^+ ion adsorption in the OMC-0 electrode as compared to OMC-2 at identical conditions.

Most surprisingly, this happens despite the fact that OMC-0 exhibits a considerably lower specific nanopore volume as compared to the activated OMC-2 material. Across all operating conditions, OMC-0 also exhibits a higher CE than OMC-2. This striking result is attributed to the higher amount of ultramicropores in OMC-0 (Fig. 1b, *Supporting Information*, Fig. S3), i.e., pores smaller than approximately 0.7 nm, which roughly corresponds to the diameter of a hydrated Cs^+ ion. This sub-nanometer confinement imposes strong steric constraints on fully hydrated ions, promoting counter-ion-adsorption as the dominant charge-balancing mechanism [21,46].

Fig. 4 shows that in the "quasi-static" limit (0.2 mL/min), the concentration change in the bulk electrolyte close to the outlet is $\Delta c \approx -12$ mM for OMC-0 but only −8 mM for OMC-2. Given the feedwater concentration of 15 mM, this means an 80 % concentration decrease in the flow channel for OMC-0 but only about 50 % for OMC-2. We interpret this by enhanced cross-electrode ion exchange for OMC-2, which limits its maximum desalination capacity. Notably, OMC-0 achieves very deep local depletion under "quasi-static" or intermediate flow conditions ($\Delta c \approx -12$ mM at the center and outlet), which may be highly relevant when maximum salt removal is the primary objective.

At the highest flow rate, X-ray-derived and conductivity-derived charge efficiencies agree well within the margin of error, which confirms the robustness of the X-ray approach under optimal replenishment. At intermediate and low flow, ex-situ conductivity can underestimate η as compared to the X-ray results because the bulk electrolyte concentration at the inlet may not have returned to its initial value at the end of the charging period, while the X-ray approach resolves the local state directly.

A closer look at the two boundary flow rates (i.e., comparing the fast flow of 14 mL/min with the "quasi-static" case of 0.2 mL/min) reveals that the X-ray-based CE decreases by about 33 % for OMC-0 and about 43 % for OMC-2. The relative drop is thus similar for both materials, suggesting that even though ionophobicity raises the absolute efficiency, it does not mitigate the flow-induced decrease of efficiency. The primary driver of parasitic pathways at low flow is insufficient ion replenishment. Even the “standard operating regime” (1.6 mL/min) yields a measurable improvement over 0.2 mL/min, which underscores the central role of replenishment. The local X-ray mapping across high-flow and "quasi-static" conditions brackets the full operating envelope of CDI CE for a given material and geometry. Unlike purely effluent-based CDI metrics, it quantifies the "quasi-static" limit in situ, separating ionophobicity-driven efficiency from replenishment-limited losses.

Comparing the stored Cs^+ concentrations at the inlet POIs from Fig. 5 with other POIs allows us to determine local differences. At 1.6 mL/min, the center and outlet are about 34 % less efficient than the inlet for both materials. This decrease is substantial and is expected to accumulate over longer electrodes. OMC-0 outperforms OMC-2 at every position (Fig. 5), which is consistent with strongly enhanced counter-ion adsorption in OMC-0.

Nevertheless, the results from Fig. 4–5 suggest that a higher local velocity promotes higher local efficiency. Therefore, a tapered flow path that increases velocity towards the outlet may lead to high desalination with a more homogeneous concentration profile along the flow path, and also reduces lateral concentration variation. However, we only state this as a hypothesis for future investigations rather than a conclusion of the current work.

Finally, we discuss another striking observation, namely the experimental observation that at the two slow flow rates some POIs show a maximum of Cs^+ in the negative electrode upon charging, with a subsequent clear decrease of the Cs^+ concentration (*Supporting Information*, Fig. S10 and Fig. S14). We believe that this effect is due to (slow) diffusive ion transport after (fast) charge balancing has been achieved in the electrode. We tentatively ascribe this effect to possible diffusive back-mixing (i.e., concomitant Cs^+ and Cl^- back diffusion into the bulk electrolyte solution). A holding-time-dependent decrease was already reported by Zhang et al. [19], and global ion concentration changes on two distinct timescales are also known from static supercapacitors [16]. Alternatively, proton-mediated ion exchange (i.e., gradual exchange of Cs^+ ions by H^+ ions) cannot be excluded. This may be particularly expected as a consequence of cumulative ionization of water due to the absorption of X-rays and potential secondary reactions involving radicals. Even pure water has been shown to exhibit considerably higher conductivity in confinement [47].

4. Conclusions

We introduced position-resolved X-ray transmission to map local concentration changes in a flow-by CDI cell under operando conditions, resolving independently the bulk electrolyte in the flow channel and at predefined points (POIs) in both electrodes. Measurements at high flow rate and at a "quasi-static" limit within the same platform cover the full operating envelope of CE and SAC for a given material and geometry. It also quantifies the "quasi-static" limit in situ, which effluent-based methods cannot access. For the chosen electrode materials, across all flow rates, higher absolute ion uptake and charge efficiency is observed which is consistent with an ionophobicity-driven contribution due to a high fraction of ultramicropores. As the flow rate is reduced, efficiency drops for both materials, indicating that replenishment limitations rather than pore chemistry dominate at low flow. Spatial analysis shows a position-dependent ion uptake along the electrode, with geometry affecting local replenishment. Future work should include the improvement of cell reproducibility and the optimization of cell geometries (e.g., tapered cells with varying flow rate), as well as variation of the inlet concentration. Moreover, the X-ray transmission methodology can easily be extended to employing (several) different X-ray energies close to absorption edges of specific elements, allowing to separate the contributions from different ions in multi-ion systems. It may also be extended to other scanning X-ray techniques exploiting modern synchrotron radiation facilities, such as scanning small-angle X-ray scattering to directly assess local concentration changes within the nanopores, or scanning X-ray fluorescence (XRF) to assess ions individually in multi-ionic systems. We explicitly acknowledge the material-scope limitations of the present work. Further investigations using other materials including carbons frequently used for CDI will be necessary to verify the generality of our approach.

CRediT authorship contribution statement

Max V. Rauscher: Writing – original draft, Visualization, Resources, Methodology, Investigation, Formal analysis, Conceptualization. **Richard Kohns:** Writing – review & editing, Resources, Investigation. **Malina Seyffertitz:** Writing – review & editing, Visualization, Investigation. **Sebastian Stock:** Writing – review & editing, Visualization. **Sylvio Haas:** Writing – review & editing, Investigation, Data curation. **Volker Presser:** Writing – review & editing. **Christian Prehal:** Writing – review & editing. **Nicola Hüsing:** Writing – review & editing, Resources. **Oskar Paris:** Writing – review & editing, Writing – original draft, Supervision, Resources, Methodology, Investigation, Conceptualization.

Declaration of competing interest

The authors declare that they have no known competing financial interests or personal relationships that could have appeared to influence the work reported in this paper.

Acknowledgements

We acknowledge DESY (Hamburg, Germany), a member of the Helmholtz Association HGF, for the provision of experimental facilities. Parts of this research were carried out at PETRA III. Data were collected using P62 SAXSMAT beamline operated by Sylvio Haas. We would like to thank Stella Gries for assistance during the experiments and Patrick Huber for fruitful discussions. Beamtime was allocated for the Targeted Challenge Driven proposal on Molecular Water Science T-20240163 EC. We also acknowledge the scientific exchange and support of the Centre for Molecular Water Science, Hamburg. The authors would also like to express their gratitude to Peter Moharitsch from the Chair of Physics at Montanuniversität Leoben for support with the design and fabrication of the operando CDI-cells, and to Gerhard Hawranek from the Chair of Physical Metallurgy and Thomas Kremmer from the Chair of Nonferrous Metallurgy (both Montanuniversität Leoben) for the help with the SEM and TEM respectively.

Appendix A. Supplementary data

Supplementary data to this article can be found online at https://doi.org/10.1016/j.desal.2026.119849.

Data availability

Data will be made available on request.

References

[1] M.A. Shannon, P.W. Bohn, M. Elimelech, J.G. Georgiadis, B.J. Mariñas, A. M. Mayes, Science and technology for water purification in the coming decades, Nature 452 (2008) 301–310, https://doi.org/10.1038/nature06599.
[2] J.J. Urban, Emerging scientific and engineering opportunities within the water-energy Nexus, Joule 1 (2017) 665–688, https://doi.org/10.1016/j.joule.2017.10.002.
[3] F.A. AlMarzooqi, A.A. Al Ghaferi, I. Saadat, N. Hilal, Application of capacitive deionisation in water desalination: a review, Desalination 342 (2014) 3–15, https://doi.org/10.1016/J.DESAL.2014.02.031.
[4] E. Jones, M. Qadir, M.T.H. Van Vliet, V. Smakhtin, S.-M. Kang, M. Qadir, The state of desalination and brine production: a global outlook, Sci. Total Environ. 657 (2019) 1343–1356, https://doi.org/10.1016/j.scitotenv.2018.12.076.
[5] J. Eke, A. Yusuf, A. Giwa, A. Sodiq, The global status of desalination: an assessment of current desalination technologies, plants and capacity, Desalination 495 (2020) 114633, https://doi.org/10.1016/j.desal.2020.114633.
[6] Y. Oren, Capacitive deionization (CDI) for desalination and water treatment — past, present and future (a review), Desalination 228 (2008) 10–29, https://doi.org/10.1016/j.desal.2007.08.005.
[7] X. Yang, J. Li, W. Qu, W. Wang, P. Wang, J. Ma, Bibliometrics and systematic reviews: recent development and prospects of electrode materials for capacitive deionization, Desalination 599 (2025) 118450, https://doi.org/10.1016/j.desal.2024.118450.
[8] S. Porada, R. Zhao, A. Van Der Wal, V. Presser, P.M. Biesheuvel, Review on the science and technology of water desalination by capacitive deionization, Prog. Mater. Sci. 58 (2013) 1388–1442, https://doi.org/10.1016/j.pmatsci.2013.03.005.
[9] N. Anh, T. Tran, T.M. Khoi, M. Ngo, H. Phuoc, J. Bin, Y. Cho, A Review of Recent Advances in Electrode Materials and Applications for Flow-electrode Desalination Systems, 2022, https://doi.org/10.1016/j.desal.2022.116037.
[10] M. Torkamanzadeh, C. Kök, P.R. Burger, P. Ren, Y. Zhang, J. Lee, C. Kim, V. Presser, Best practice for electrochemical water desalination data generation and analysis, Cell Rep. Phys. Sci. (2023) 101661, https://doi.org/10.1016/j.xcrp.2023.101661.
[11] Ruihua Zhao, R. Zhao, P.M. Biesheuvel, P.M. Biesheuvel, Hme Miedema, H. Miedema, H. Brüning, H. Bruning, H. Bruning, A. van der Wal, A. van der Wal, Charge efficiency: a functional tool to probe the double-layer structure inside of porous electrodes and application in the modeling of capacitive deionization, J. Phys. Chem. Lett. 1 (2010) 205–210, https://doi.org/10.1021/jz900154h.
[12] R.A.W. Dryfe, J.M. Griffin, Capacitive de-ionisation: an electrochemical perspective, Curr. Opin. Electrochem. 35 (2022), https://doi.org/10.1016/j.coelec.2022.101084.
[13] P.M. Biesheuvel, M.Z. Bazant, Nonlinear dynamics of capacitive charging and desalination by porous electrodes, Phys. Rev. E 81 (2010) 031502, https://doi.org/10.1103/physreve.81.031502.
[14] J. Nordstrand, L. Zuili, J. Dutta, Fully 3D modeling of electrochemical deionization, ACS Omega 8 (2023) 2607–2617, https://doi.org/10.1021/acsomega.2c07133.
[15] J. Nordstrand, J. Dutta, Langmuir-based modeling produces steady two-dimensional simulations of capacitive deionization via relaxed adsorption-flow coupling, Langmuir 38 (2022) 3350–3359, https://doi.org/10.1021/acs.langmuir.1c02806.
[16] C. Prehal, C. Koczwara, H. Amenitsch, V. Presser, O. Paris, Salt concentration and charging velocity determine ion charge storage mechanism in nanoporous supercapacitors, Nat. Commun. 9 (2018), https://doi.org/10.1038/s41467-018-06612-4.
[17] M. Seyffertitz, S. Stock, M.V. Rauscher, C. Prehal, S. Haas, L. Porcar, O. Paris, Are SAXS and SANS suitable to extract information on the role of water for electric double-layer formation at the carbon - aqueous electrolyte interface? Faraday Discuss. (2023) https://doi.org/10.1039/d3fd00124e.
[18] C. Prehal, D. Weingarth, E. Perre, R.T. Lechner, H. Amenitsch, O. Paris, V. Presser, Tracking the structural arrangement of ions in carbon supercapacitor nanopores using in situ small-angle X-ray scattering, Energ. Environ. Sci. 8 (2015) 1725–1735, https://doi.org/10.1039/c5ee00488h.
[19] Y. Zhang, P. Ren, Y. Liu, V. Presser, Particle size distribution influence on capacitive deionization: insights for electrode preparation, Desalination 525 (2022), https://doi.org/10.1016/J.DESAL.2021.115503.
[20] M. Thommes, K. Kaneko, A.V. Neimark, J.P. Olivier, F. Rodriguez-Reinoso, J. Rouquerol, K.S.W. Sing, Physisorption of gases, with special reference to the evaluation of surface area and pore size distribution (IUPAC technical report), Pure Appl. Chem. 87 (2015) 1051–1069, https://doi.org/10.1515/pac-2014-1117.
[21] Y. Zhang, C. Prehal, H. Jiang, Y. Liu, G. Feng, V. Presser, Ionophobicity of carbon sub-nanometer pores enables efficient desalination at high salinity, Cell Rep. Phys. Sci. 3 (2022), https://doi.org/10.1016/J.XCRP.2021.100689.
[22] Sheng Bi, Yuan Zhang, Luca Cervini, Tangming Mo, John M. Griffin, Volker Presser, Guang Feng, Permselective ion electrosorption of subnanometer pores at high molar strength enables capacitive deionization of saline water, sustain, Energy Fuel 4 (2020) 1285–1295, https://doi.org/10.1039/c9se00996e.
[23] C. Merlet, C. Péan, B. Rotenberg, P.A. Madden, B. Daffos, P.-L. Taberna, P. Simon, M. Salanne, Highly confined ions store charge more efficiently in supercapacitors, Nat. Commun. 4 (2013) 2701, https://doi.org/10.1038/ncomms3701.
[24] M.R. Cerón, F. Aydin, S.A. Hawks, D.I. Oyarzun, C.K. Loeb, A. Deinhart, C. Zhan, T. A. Pham, M. Stadermann, P.G. Campbell, Cation selectivity in capacitive deionization: elucidating the role of pore size, electrode potential, and ion dehydration, ACS Appl. Mater. Interfaces 12 (2020) 42644–42652, https://doi.org/10.1021/acsami.0c07903.
[25] S. Zavahir, T. Elmakki, M. Gulied, Z. Ahmad, L. Al-Sulaiti, H.K. Shon, Y. Chen, H. Park, B. Batchelor, D.S. Han, A review on lithium recovery using electrochemical capturing systems, Desalination 500 (2021) 114883, https://doi.org/10.1016/j.desal.2020.114883.
[26] H. Liu, L. Tong, M. Su, D. Chen, G. Song, Y. Zhou, The latest research trends in the removal of cesium from radioactive wastewater: a review based on data-driven and visual analysis, Sci. Total Environ. 869 (2023) 161664, https://doi.org/10.1016/j.scitotenv.2023.161664.
[27] Z. Wang, P. Ye, Z. Liang, Z. Chen, F. Yang, Y. Bando, L. Deng, Unraveling the role of field strength on Sr2+ removal in flow-electrode capacitive deionization systems, Sep. Purif. Technol. 372 (2025) 133432, https://doi.org/10.1016/j.seppur.2025.133432.
[28] M. Dai, L. Xia, S. Song, C. Peng, J.R. Rangel-Mendez, R. Cruz-Gaona, Electrosorption of as(III) in aqueous solutions with activated carbon as the electrode, Appl. Surf. Sci. 434 (2018) 816–821, https://doi.org/10.1016/j.apsusc.2017.10.238.
[29] C. Koczwara, S. Rumswinkel, L. Hammerschmidt, M. Salihovic, M.S. Elsaesser, H. Amenitsch, O. Paris, N. Huesing, Nanofibers versus Nanopores: a comparison of the electrochemical performance of hierarchically ordered porous carbons, ACS Appl. Energy Mater. 2 (2019) 5279–5291, https://doi.org/10.1021/acsaem.9b01035.
[30] S. Liu, V.Q. Do, K.C. Smith, Modeling of electrochemical deionization across length scales: recent accomplishments and new opportunities, Curr. Opin. Electrochem. 22 (2020) 72–79, https://doi.org/10.1016/j.coelec.2020.05.003.
[31] C. Prehal, C. Koczwara, N. Jäckel, A. Schreiber, M. Burian, H. Amenitsch, M. A. Hartmann, V. Presser, O. Paris, Quantification of ion confinement and desolvation in nanoporous carbon supercapacitors with modelling and in situ X-ray scattering, Nat. Energy 2 (2017) 1–8, https://doi.org/10.1038/nenergy.2016.215.
[32] S. Goutham, A. Keerthi, A. Ismail, A. Bhardwaj, H. Jalali, Y. You, Y. Li, N. Hassani, H. Peng, M.V.S. Martins, F. Wang, M. Neek-Amal, B. Radha, Beyond steric selectivity of ions using ångström-scale capillaries, Nat. Nanotechnol. 18 (2023) 596–601, https://doi.org/10.1038/s41565-023-01337-y.
[33] K. Sharma, Y.-H. Kim, J. Gabitto, R.T. Mayes, S. Yiacoumi, H.Z. Bilheux, L.M. H. Walker, S. Dai, C. Tsouris, Transport of ions in mesoporous carbon electrodes during capacitive deionization of high-salinity solutions, Langmuir 31 (2015) 1038–1047, https://doi.org/10.1021/la5043102.
[34] A. Hemmatifar, M. Stadermann, J.G. Santiago, Two-dimensional porous electrode model for capacitive deionization, J. Phys. Chem. C 119 (2015) 24681–24694, https://doi.org/10.1021/acs.jpcc.5b05847.
[35] H.G. Steinrück, General relationship between salt concentration and x-ray absorption for binary electrolytes, AIP Adv. 11 (2021), https://doi.org/10.1063/5.0072947.

[36] K. Sharma, H.Z. Bilheux, L.M.H. Walker, S. Voisin, R.T. Mayes, J.O.K. Jr, S. Yiacoumi, D.W. DePaoli, S. Dai, C. Tsouris, Neutron imaging of ion transport in mesoporous carbon materials, Phys. Chem. Chem. Phys. 15 (2013) 11740–11747, https://doi.org/10.1039/C3CP51310F.
[37] M.V. Rauscher, M. Seyffertitz, R. Kohns, S. Stock, H. Amenitsch, N. Huesing, O. Paris, Optimizing surfactant removal from a soft-templated ordered mesoporous carbon precursor: an in situ SAXS study, J. Appl. Cryst. 56 (2023) 801–809, https://doi.org/10.1107/S1600576723003886.
[38] G. Hasegawa, K. Kanamori, T. Kiyomura, H. Kurata, T. Abe, K. Nakanishi, Hierarchically porous carbon monoliths comprising ordered mesoporous Nanorod assemblies for high-voltage aqueous supercapacitors, Chem. Mater. 28 (2016) 3944–3950, https://doi.org/10.1021/acs.chemmater.6b01261.
[39] G.Yu. Gor, M. Thommes, K.A. Cychosz, A.V. Neimark, Quenched solid density functional theory method for characterization of mesoporous carbons by nitrogen adsorption, Carbon 50 (2012) 1583–1590, https://doi.org/10.1016/j.carbon.2011.11.037.
[40] P.I. Ravikovitch, A. Vishnyakov, R. Russo, A.V. Neimark, Unified approach to pore size characterization of microporous carbonaceous materials from N2, Ar, and CO2 adsorption isotherms, Langmuir 16 (2000) 2311–2320, https://doi.org/10.1021/la991011c.
[41] S. Haas, X. Sun, A.L.C. Conceição, J. Horbach, S. Pfeffer, The new small-angle X-ray scattering beamline for materials research at PETRA III: SAXSMAT beamline P62, J. Synchrotron Radiat. 30 (2023) 1156–1167, https://doi.org/10.1107/S1600577523008603.
[42] G.A. Zickler, S. Jähnert, W. Wagermaier, S.S. Funari, G.H. Findenegg, O. Paris, Physisorbed films in periodic mesoporous silica studied by in situ synchrotron small-angle diffraction, Phys. Rev. B - Condens. Matter Mater. Phys. 73 (2006), https://doi.org/10.1103/PhysRevB.73.184109.
[43] K. Laxman, A. Husain, A. Nasser, M. Al Abri, J. Dutta, Tailoring the pressure drop and fluid distribution of a capacitive deionization device, Desalination 449 (2019) 111–117, https://doi.org/10.1016/J.DESAL.2018.10.021.
[44] P.M. Biesheuvel, S. Porada, M. Levi, M.Z. Bazant, Attractive forces in microporous carbon electrodes for capacitive deionization, J. Solid State Electrochem. 18 (2014) 1365–1376, https://doi.org/10.1007/s10008-014-2383-5.
[45] J. Nordstrand, J. Dutta, Simplified prediction of ion removal in capacitive deionization of multi-ion solutions, Langmuir 36 (2020) 1338–1344, https://doi.org/10.1021/acs.langmuir.9b03571.
[46] S. Kondrat, A.A. Kornyshev, When hard work pays off, Nanoscale Horiz. (2025), https://doi.org/10.1039/D5NH90052B.
[47] V.G. Artemov, Dynamical conductivity of confined water, Meas. Sci. Technol. 28 (2016) 014013, https://doi.org/10.1088/1361-6501/28/1/014013.
[48] C.T. Chantler, K. Olsen, J. Dragoset, J. Chang, A.R. Kishore, S.A. Kotochigova, D. S. Zucker, X-Ray Form Factor, Attenuation and Scattering Tables (Version 2.1). http://physics.nist.gov/ffast, 2005 (accessed March 24, 2025).